Design and Evaluation of a Quasi-Passive Variable Stiffness Prosthesis for Walking Speed Adaptation in People With Transtibial Amputation

Emily Rogers-Bradley, Seong Ho Yeon, Christian Landis, and Hugh M. Herr

***Abstract*—The biological ankle joint adjusts stiffness to adapt to changing walking speed, terrain, and load carriage. The most commonly used passive transtibial prostheses are unable to adjust device stiffness and therefore do not maximize potential energy storage and peak prosthesis power across speeds. We present a quasi-passive variable stiffness ankle–foot prosthesis with discrete stiffness adjustment from 352 to 479 Nm/radian, corresponding to the range of biological ankle quasi-stiffness exhibited during level ground walking at speeds from 0.75 to 1.5 m/s for a 77 kg person. We implement a novel parallel leaf spring mechanism that utilizes custom solenoid-driven linear actuators to constrain sliding of parallel leaf springs relative to a mechanical ground in order to control bending stiffness. The prosthesis is lower in mass than all existing variable stiffness prostheses, with a mass of 945 g. We present initial results from a pilot study with one participant with unilateral transtibial amputation, demonstrating an increase in range of motion, peak prosthesis power, and energy storage and return, and a decrease in contralateral knee external adduction moment across a range of walking speeds. This variable stiffness ankle–foot prosthesis demonstrates the potential to improve biomechanics of walking through the design of a low-mass, quasi-passive prosthesis.**

***Index Terms*—Quasi-passive prosthesis, variable stiffness mechanism, wearable robotics.**

Manuscript received 26 October 2022; revised 13 April 2023; accepted 11 May 2023. Recommended by Technical Editor Hiroyuki Ishii and Senior Editor Hong Qiao. This work was supported in part by the National Science Foundation Graduate Research Fellowship under Grant 1122374, and in part by the Massachusetts Institute of Technology (MIT) Media Laboratory Consortia. *(Corresponding author: Emily Rogers-Bradley.)*

This work involved human subjects or animals in its research. Approval of all ethical and experimental procedures and protocols was granted by the Massachusetts Institute of Technology Committee on the Use of Humans as Experimental Subjects under Application No. 1609692618, and performed in line with the Declaration of Helsinki.

Emily Rogers-Bradley was with the Massachusetts Institute of Technology, Cambridge, MA 02142 USA. She is now with the University of Calgary, Calgary, AB T2L 1Y6, Canada (e-mail: emily.rogersbradley@ucalgary.ca).

Seong Ho Yeon, Christian Landis, and Hugh M. Herr are with the Massachusetts Institute of Technology, Cambridge, MA 02142 USA (e-mail: syeon@mit.edu; clandis@media.mit.edu; hherr@media.mit.edu).

Color versions of one or more figures in this article are available at https://doi.org/10.1109/TMECH.2023.3276710.

Digital Object Identifier 10.1109/TMECH.2023.3276710

I. Introduction

CURRENTLY there are an estimated 875 000 people with major lower limb loss in the United States, with numbers projected to increase 1.6-fold by 2050 due to increasing prevalence of diabetes, obesity, and related dysvascular conditions [1]. Lower limb amputation often leads to secondary conditions such as osteoarthritis, osteopenia, back pain, postural changes, and general deconditioning [2]. For people with unilateral transtibial amputation (TTA), prevalence of knee osteoarthritis (OA) in the contralateral (sound) limb is 17× higher than in the general population, affecting 27% of people with unilateral TTA [3]. This large increase in prevalence of knee OA is likely due to increasing knee external adduction moment (EAM) on the contralateral side, as the magnitude of EAM during walking has been shown to be a strong predictor of knee OA development [4], [5], [6], [7]. This increase in contralateral limb loading is hypothesized to be due to decreased pushoff power from the prosthesis side during step transitions [6]. A key property of the biological ankle–foot complex which is not reproduced in passive energy storage and return (ESR) prostheses, the most widely used type of prosthesis for people with TTA, is variable joint stiffness [15]. Ankle quasi-stiffness is modulated based on walking speed, terrain, and body mass [16]. Fig. 1 shows the joint moment of the biological ankle over a range of joint angles during standing and walking at various speeds. The slope of the dashed lines represents the quasi-stiffness of the biological ankle for each speed, demonstrating the increase in quasi-stiffness of the ankle as walking speed increases [8], [9]. This modulation of joint compliance contributes to efficient power generation and energy storage in the ankle [15], [17]. Few devices exist that allow for active adjustment of prosthetic joint stiffness. However, it has been demonstrated that for prosthetic devices of a fixed joint stiffness, lower stiffness increases range of motion, increases energy storage and return, and increases peak power from the prosthesis [18], [19], [20]. An increase in peak power generation from the prosthesis is associated with decreased loading on the contralateral limb and decreased knee EAM, potentially leading to lower rates of contralateral limb knee OA in the long term [6], [21]. We hypothesize that through the implementation of a variable stiffness prosthesis, energy storage and peak prosthesis power can be increased across a range of walking speed, leading to decreased unwanted loading on the contralateral limb. This research aims to explore how we can restore the benefits of

TABLE I
VARIABLE STIFFNESS ANKLE–FOOT PROSTHESES PROPERTIES

Category	Device	Mass (g)	Build height (mm)	Stiffness range (Nm/rad)	Function
Quasi-passive	**Rogers-Bradley et al.**	**945**	**162**	**352–479**	**Discrete stiffness adjustment**
	Shepherd et al. [10]	1078	–	39–527	Continuous stiffness adjustment
	Lee et al. [11]	1107	170	348-376	Continuous stiffness adjustment
	Lecomte et al. [12]	1330	179	487-602	Continuous stiffness adjustment
	Collins et al. [13]	1370	129	–	Energy recycling
Powered	Heremans et al. [14]	1380	110	240–428	SEA variable stiffness parallel spring

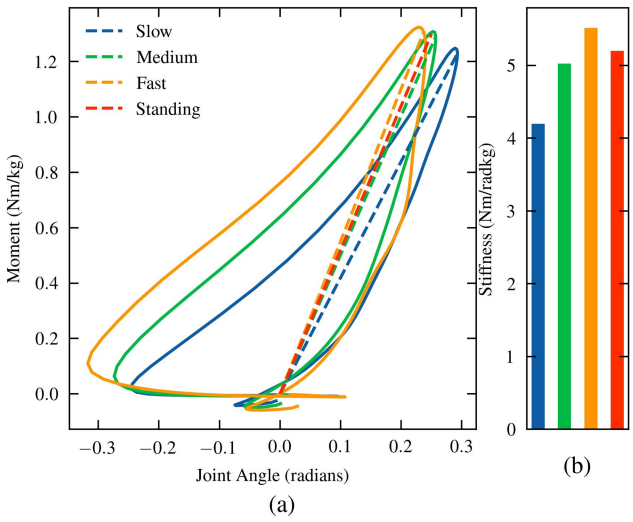

Fig. 1. Stiffness of biological ankle during walking. (a) Moment/angular displacement curve of the biological ankle during walking at various speeds (data from [8], [9]), (b) corresponding quasi-stiffness of ankle.

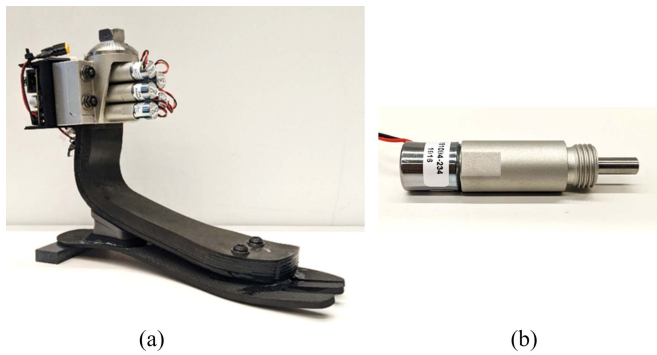

Fig. 2. Variable stiffness ankle–foot prosthesis prototype. (a) Final VSA prosthesis prototype including composite carbon fiber leaf springs, solenoid driven linear actuators, actuator housing, and custom embedded system. (b) Solenoid driven linear actuator controls engagement of pin with slot in leaf springs to constrain relative sliding of springs in order to increase total device bending stiffness.

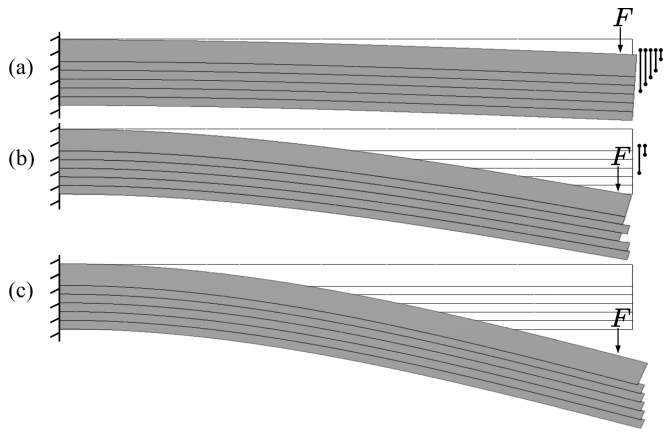

Fig. 3. Stiffness mechanism. Parallel leaf spring stiffness changing mechanism implemented in the variable stiffness prosthesis. By either locking parallel spring to a ground spring or allowing them to freely slide, bending stiffness is discretely adjusted from a range of (a) high stiffness configuration with all parallel springs locked to ground spring, (b) intermediate stiffness levels in which one or multiple springs are allowed to freely slide relative to the ground spring, and (c) lowest stiffness configuration in which all springs are unlocked and able to slide relative to ground spring.

variable joint compliance exhibited in the biological ankle while maintaining low device mass, low build height, and low power requirements. To achieve this goal we are interested in the potential of quasi-passive prostheses—devices that use electrical energy to change device state or mechanical behavior, but do not perform net positive work on the user during walking. Due to their lower power requirements, quasi-passive devices are able to be designed with lower device mass, complexity, size, auditory noise, and cost than fully powered systems. Existing devices that aim to mimic the stiffness modulation of a biological ankle include quasi-passive devices that vary joint stiffness [10], [11], [12] or recycle heel strike energy during pushoff [13], and powered devices that combine a stiffness-adjustable parallel spring with a series-elastic actuator [14] (Table I). Additional quasi-passive prostheses exist that vary damping properties [22], [23], [24], [25], joint position [26], [27], [28], spring equilibrium set-point [29], and forefoot bending stiffness [30]. This article presents the mechanical and mechatronic design of a novel quasi-passive variable stiffness ankle–foot prosthesis (VSA) for walking speed adaptation that is lower in mass than all existing variable stiffness ankle–foot prostheses (Fig. 2). We present the device design, characterization, and benchtop device validation of the prosthesis. We present initial results from a pilot study with one study participant that demonstrate device functionality while walking at variable speeds, showing promising initial results on the ability to increase peak power and decrease contralateral limb loading through a variable stiffness prosthesis. These preliminary results will inform future studies to further assess the

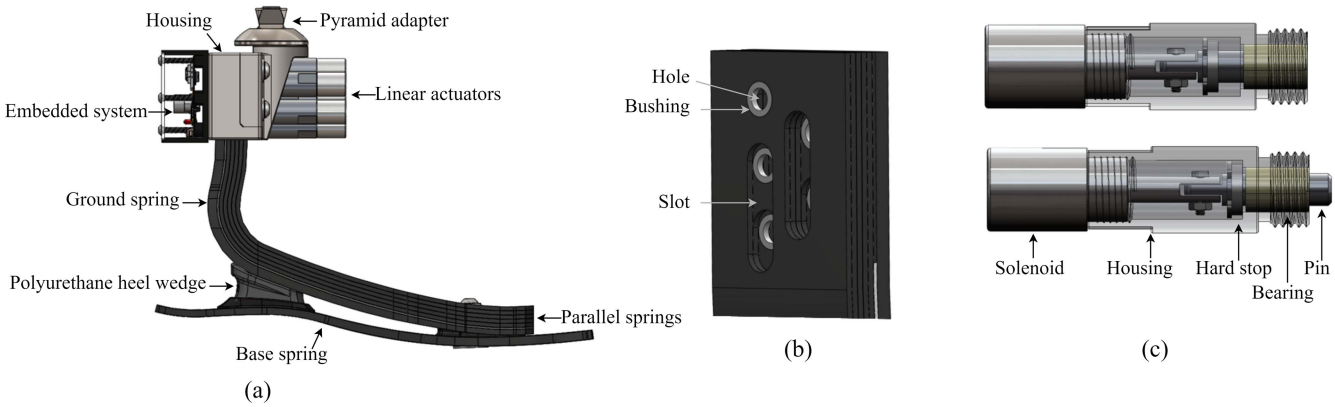

Fig. 4. Variable stiffness ankle–foot prosthesis design. (a) VSA prosthesis consisting of five parallel independently controlled leaf springs and a ground spring, a base spring, a polyurethane heel wedge, linear actuators, structural housing, standard prosthetic pyramid adaptor, and custom embedded system, (b) detailed view of internal spring structure showing slots, holes, and bushing, (c) linear actuator overview showing solenoid, housing, hard stop, bearing, and pin.

impact and efficacy of the variable stiffness prosthesis in a larger clinical study.

II. Device Design

This section describes the mechanical design of the variable stiffness prosthesis, linear actuators, and electronics and software design. The device parameters are outlined in Table I. The total device mass including battery and electronics is 945 g, the build height is 162 mm, and the stiffness range is 352–479 Nm/rad. The device is designed for a maximum user weight of 88 kg, has an estimated battery life of 11 h, and an estimated cycle life of 2.0×10^6 steps. The prosthesis (Fig. 4) consists of the following subsystems:

1) composite leaf springs;
2) mechanical housing;
3) linear actuators.

The prosthesis interfaces with a standard prosthetic socket via a pyramid adapter. The following subsections outline the working principle of the stiffness change mechanism, the design of the carbon fiber leaf springs, mechanical housing design, actuator development, and control system and electronics design.

A. Stiffness Change Mechanism

The variable stiffness prosthesis utilizes a novel stiffness changing mechanism in which computer-controlled solenoid driven microlinear actuators lock relative sliding between parallel composite leaf-springs, increasing the bending stiffness. Fig. 3 demonstrates the working principle behind this design. The system consists of a ground spring and five parallel springs, which in the stiffest configuration [Fig. 3(a)] are prevented from sliding relative to the ground spring, increasing bending stiffness. A number of intermediate stiffness configurations exist [Fig. 3(b)], in which one or multiple springs are locked to the ground spring. In the lowest stiffness configuration [Fig. 3(c)], all springs are free to slide relative to the ground spring. The locking of each parallel leaf spring is independently controlled, such that the total number of distinct stiffness configurations for the device with one ground spring and five parallel springs is equal to 32, as shown in (2). This characteristic is governed by the parallel axis theorem (1), where I_c is the centroidal moment of inertia, A is the cross-sectional area, and d is the distance between the centroidal axis and the bending axis. The bending moment of inertia for springs farther from the centroidal axis is greater than spring closer, such that locking spring 1 to ground is stiffer than locking spring 5 to ground and each distinct combination of locked/unlocked springs has a different bending stiffness. The device architecture has several key functionalities that distinguish it from existing devices. The locking mechanism architecture allows for rapid state changes between stiffnesses, with a constant state transition time of <10 ms regardless of the size of stiffness increase. The multileaf spring architecture enables stiffness control with actuation perpendicular to the direction of bending, allowing for much lower stiffness and force actuators than would be necessary in an architecture that requires changing distance between parallel springs. The binary state of the solenoid driven actuators allows for robust control of device properties in a simple actuator package, and the implementation of magnetic locking solenoids necessitates no additional holding energy in the extended or retracted position of the actuators.

$$I_{\text{parallel}} = I_c + Ad^2 \tag{1}$$

$$n_{\text{combinations}} = \sum_{n=0}^{5} C(5, i) = 32. \tag{2}$$

B. Leaf Spring Design

The leaf spring subsystem consists of a ground spring and five parallel leaf springs. Parallel leaf springs are 1.742 mm thick (13 plies), and the ground spring is tapered with a thickness of 4.96 mm (37 plies) at the proximal end and 2.95 mm (22 plies) at the distal end. The custom leaf springs were fabricated (Ottobock Manufacturing, Ottobock, Salt Lake City,

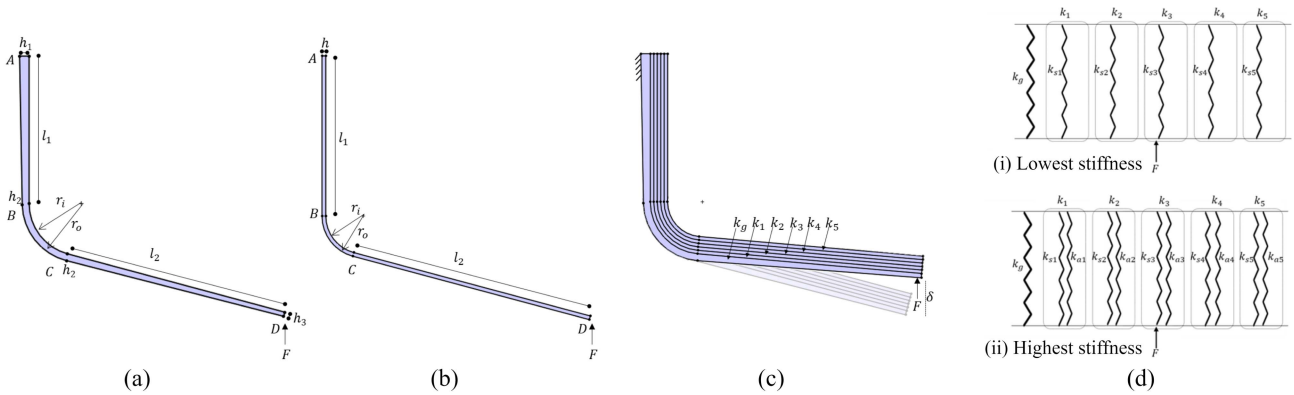

Fig. 5. Parametric model of spring stiffness. (a) Simplified model of base spring geometry showing variables of interest, leaf springs are modeled as straight cantilever beam section AB, curved section BC, and straight cantilever beam section CD, (b) parallel spring geometry, (c) total spring assembly, (d) spring stiffness model of unlocked (lowest stiffness) and locked (highest stiffness) device states.

UT, USA) using unidirectional carbon fiber sheets with a ply thickness of 0.134 mm. Between each spring a layer of PTFE with a thickness of 0.127 mm is co-cured to the springs to decrease the coefficient of friction between the sliding surfaces.

1) Parametric Model of Leaf Spring: We developed a parametric model in order to evaluate the stiffness of the device for a given spring geometry, as well as the expected stiffness increase when each spring is locked. Using Castigliano's Theorem, we calculated the stiffness of the curved springs by taking the partial derivative of the strain energy with respect to force [31]. We modeled the geometry of the leaf springs as straight cantilever beam section in series with a curved section [Fig. 5(a) and (b)]. For the straight portion of the springs the deflection of the spring under load F is calculated in (3), where E is the bulk elastic modulus of the composite material, I is the moment of inertia, M is the bending moment, and A is the cross-sectional area. Bending moment of inertia, I, and cross-sectional area, A, of the ground spring vary along length l, as the spring is tapered.

$$\delta = \int_0^l \frac{1}{EI}\left(M\frac{\partial M}{\partial F}\right)dx + \int_0^l \frac{1}{AE}\left(F\frac{\partial F}{\partial F}\right)dx. \tag{3}$$

We calculate deflection of curved section BC as the partial derivative of the strain energy in terms of force, F, integrated over θ from 0 to $\pi/4$ (4), where M is bending moment, E is modulus of elasticity, and e is eccentricity. The geometric parameters are shown in Fig. 5 for the ground spring [Fig. 5(a)] and the parallel springs [Fig. 5(b)].

$$\delta = \int_0^{\pi/4} \frac{M}{AeE}\left(\frac{\partial M}{\partial F}\right)d\theta + \int_0^{\pi/4} \frac{F_\theta R}{AE}\left(\frac{\partial F_\theta}{\partial F}\right)d\theta - \int_0^{\pi/4} \frac{1}{AE}\frac{\partial (MF_\theta)}{\partial F}d\theta + \int_0^{\pi/4} \frac{CF_r R}{AG}\left(\frac{\partial F_r}{\partial F}\right)d\theta. \tag{4}$$

The total stiffness of the system in the lowest stiffness configuration is modeled as a parallel spring configuration with the ground spring parallel to the five parallel springs, shown in Fig. 5(d) (5). The stiffness of the locked actuator is calculated in (6), where the actuator stiffness is equivalent to the stiffnesses of the bushing (k_{bearing}), the shaft (k_{shaft}), and the pin/slot interface ($k_{\text{interface}}$) in series. When the pin is locked, the stiffness of each subsystem increases, with the actuator added in parallel with its corresponding leaf spring, shown in Fig. 5(d) (7). Equation 8 calculates δ_{ratio}, where $\theta_{\text{deflection}}$ is the angular deflection of the distal end of the spring, r_o is the outer radius of the spring, r_i is the inner radius, and l_2 is the length of the distal segment of the spring.

$$k_{\text{unlocked}} = k_{\text{ground}} + k_1 + k_2 + k_3 + k_4 + k_5 \tag{5}$$

$$k_{\text{actuator}} = \left(\frac{1}{k_{\text{bearing}}} + \frac{1}{k_{\text{shaft}}} + \frac{1}{k_{\text{interface}}}\right)^{-1} \tag{6}$$

$$k_{\text{locked}} = k_{\text{ground}} + \sum_{n=1}^{5} k_{s(n)} + \sum_{n=1}^{5} \delta_{\text{ratio}} k_{\text{actuator}} \tag{7}$$

$$\delta_{\text{ratio}} = \frac{\delta_{\text{proximal}}}{\delta_{\text{distal}}} = \frac{\sin^{-1}\left(\frac{\delta_{\text{distal}}}{l_2}\right)(r_o - r_i)}{\delta_{\text{distal}}}. \tag{8}$$

2) Finite Element Modeling of Leaf Springs: We modeled stiffness and structural properties of the composite leaf springs in Ansys Composite PrepPost (ACP, Ansys, Inc., Canonsburg, PA, USA) finite element analysis (FEA) software. We built an FEA model representing the ply geometry and fiber orientation of the leaf springs. Bonded contacts are used at the toe to simulate the epoxy joint, and between the ground spring and the housing. Frictional contacts are used at the sliding surface of each spring, with a coefficient of friction of 0.10. The model is set to large deflection mode, weak springs is turned OFF, and 100 steps are used. The housing is a fixed support and a ramped vertical load of 700 N is applied to the toe of the prosthesis to replicate the benchtop test conducted during device validation. We performed fatigue analysis to ensure the carbon fiber will likely withstand cyclic loading of up to 2 million cycles at our expected load, in order to meet the ISO standards for cycle life [32]. The maximum expected stress in the carbon fiber springs was calculated as 500 MPa as an upper bound using standard beam bending equations, and our Ansys FEA model predicts a maximum stress of 350 MPa. Experimental data form the literature indicates a

fatigue limit of 1250 MPa for unidirectional 0° carbon fiber at 10^7 cycles [33], [34]. This gives us a factor of safety (FOS) of 5.95 at our max expected loading, indicating that based on these preliminary conservative calculations a fatigue failure of the carbon fiber springs is unlikely.

3) Contact Stress At Spring Interface: We modeled the contact loading at the interface between the parallel springs, a contact area of the PTFE coating to carbon fiber. The contact stress at the interface between the springs is analyzed based on contact mechanics of sliding. This loading can be described as a normal force pressing the springs together as well as a frictional force due to the relative sliding between the springs. As the thin PTFE film is less than five times the half-width of the contact area, the stiffness of the contact is not affected by the film and can be treated as two equal stiffness carbon fiber components in contact [32]. The spring interface is approximated as a cylinder on a flat plate, the half width of contact is calculated based on Herztian contact. The maximum contact stress at the spring interface is estimated to be 1.06 MPa, for a safety factor of 38× above the yield stress of the epoxy in the composite. This analysis demonstrates that the bending stress dominates in the carbon fiber and contact stress is not a concern.

4) Interspring Wear At PTFE Interface: We calculated the expected sliding wear rate of the PTFE film at the sliding contact area between the leaf springs. We calculated the wear depth per operating cycle as in (9), where W is the wear rate (mm^3/Nm), l is the sliding distance per cycle (m), and P is the contact pressure at the interface (MPa). The wear rate, W, of PTFE is $35 \times 10^{-5}\text{mm}^3/\text{Nm}$ [35]. The worst-case wear scenario is calculated assuming a contact area equal to the Hertzian line contact, with a contact stress of 0.29 MPa as calculated in the previous section. For this worst-case scenario, the wear thickness per cycle is 1.02×10^{-7} mm, and the expected lifetime is 1.9×10^6 cycles.

$$t_{\text{wear}} = WlP. \tag{9}$$

C. Housing Design

The prosthesis housing is fabricated from 7075 aluminum. The base spring is bonded to the housing with an adhesive and bolted joint. A pyramid adapter is mounted on the front of the housing, allowing the prosthesis to be mounted to a prosthetic socket via standard mounting hardware.

1) FEA of Housing: We performed FEA on all structural components of the system using SolidWorks Simulation (SolidWorks, Dassault Systems, Vélizy-Villacoublay, France). We used a static structural analysis with a load of 1.5× body mass. We determined that the maximum stress in the housing components is lower than the fatigue limit of 7075 aluminum for 2×10^6 cycles.

2) Bolted Joint Design: The bolted joint between the anterior and posterior housing components as well as the bolted joint between the pyramid adapter and housing were analyzed to determine sufficient joint strength for our expected loads.

D. Actuator Design

The linear actuators are driven by a solenoid (STA-50M-STA 151094-234, Johnson Electric, Hong Kong, China) which drives an attached shaft to an extended or contracted state. The solenoid driven architecture allow for rapid changing between binary states. The pins engage with a slot on each parallel spring, when the pin is engaged is prevents the corresponding spring from sliding relative to the base spring, increasing the bending stiffness.

1) Bearing Selection: A sleeve bearing (iGlide P210, igus, Inc., Rumford, RI, USA) supports the end of the pin within the actuator housing. The bearing was selected in order to support the loads induced from the loading of the spring while the pin is engaged, the polymer bearing is preferable to a metal bearing due to the intermittent motion of this application. A Hertzian model of line contact was used to calculate the maximum expected contact stress on the bearing as 35 MPa [36]. We selected the bearing based on this expected load and the unique requirements of intermittent motion and intermittent load application.

2) Solenoid Selection: The linear actuators are driven by a solenoid (STA-50M-STA 151094-234, Johnson Electric, Hong Kong, China). The use of magnetic latching solenoids allows this mechanism to be implemented in a low-energy method. Energy consumption in both the extended and retracted position of the solenoids is minimal. The solenoid has an output force of 2 N, a stroke length of 2.5 mm, and a no-load speed of 6 ms/2.5 mm. These solenoids, with a minimum operating voltage of 6 V, consume electrical current lower than 1 A during transient transitions. The transient actuation of the actuators occurs within a duration of less than 10 ms for bilinear state transitions at an operating voltage of 14.8 V.

3) Contact Stress At Pin–Slot Interface: We modeled the contact stress at the interface between the locking pins and the slots in the carbon fiber leaf springs. We calculated the portion of the total load seen by the pin–slot interface during loading by the stiffness ratio between each parallel spring and the total stiffness from our parametric stiffness model. The portion of the total load seen by each spring is equivalent to the total load times the stiffness ratio of the spring of interest to the total stiffness. When the pin is locked, the actuator–pin–slot assembly for each spring subsystem is configured in series, such that the load seen at each pin–slot interface is equivalent to the stiffness ratio between the actuator assembly and the corresponding spring. In order to calculate the maximum stress at the contact area between the pin and slot, the Hertzian theorem of line contact is used. We calculate an estimated contact stress of 110 MPa, which gives us a safety factor of 3.8 above the yield stress of 4140 PH steel.

E. Control System Modeling and Electronics Design

We designed and implemented a custom embedded system to drive the solenoid actuators, interface with the onboard sensors, and run closed-loop control. The custom embedded system allows for more efficient, faster, and more accurate control of the prosthesis compared to utilizing traditional motor drivers due to the unique electromechanical properties of the variable

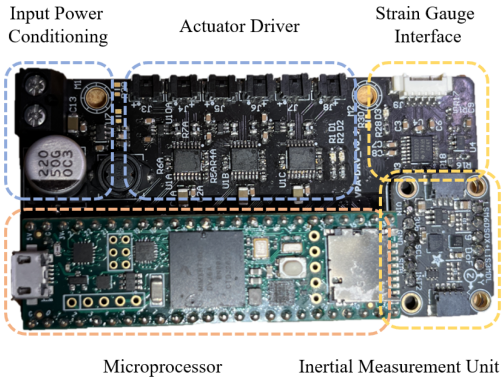

Fig. 6. Embedded system. Prototype of the designed and fabricated embedded system for VSA.

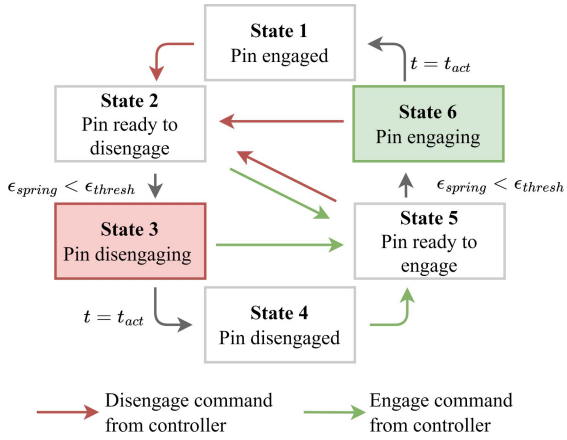

Fig. 7. Low-level finite state machine of the VSA driver. The control scheme for the actuator is designed to be energy efficient, and power is only consumed when the actuator is actively engaging in State 6 (green) or disengaging in State 3 (red). In States 1, 2, 4, and 5 (gray), the device architecture enables the actuator to hold its position without requiring any additional power. This approach optimizes power consumption and ensures that the actuator consumes energy only when necessary, thus improving the overall energy efficiency of the system.

stiffness prosthesis. Compared to standard powered prostheses, the variable stiffness prosthesis has greater controllable degrees of freedom (five), lower current requirements (<1 A), and a faster transient response time (<10 ms), motivating the implementation of a custom system.

1) Approximation of Actuator Dynamics: Due to the complex electromechanical dynamics of the actuators, closed-loop control of the actuators' mechanical states would require high-bandwidth control (>10 kHz) and accurate sensing of the actuator's dynamics. In order to minimize implementation complexity, we developed a simplified model of actuator dynamics that utilizes a constant input voltage and a fixed actuation time for each direction of actuation. The actuation time in this model is empirically determined based on the measured minimum duration required for the actuator to change its mechanical state during experimentation. This approach enables us to achieve a reasonable level of control precision while minimizing resource requirements, and allows for the desired performance of the mechatronic system without the need for additional mechanical state sensing and high bandwidth control.

2) Embedded System Hardware: The hardware design of the custom embedded system (Fig. 6) prioritized the unique characteristics of the actuators, scalability for compatibility with future iterations, incorporating multiple sensors to enable thorough analysis of system behaviors, and providing a user-friendly interface for researchers. The embedded system employs three dual channel motor driver chips (DRV8847PWR, Texas Instruments, Dallas, TX, USA) to control five solenoid actuators, each with a maximum root-mean-square (RMS) current of 1 A. An extra output channel allows for the use of additional actuators in future iterations. A serial current sensing resistor (10 mOhm) and an instrumental amplifier (INA186A3, Texas Instruments, Dallas, TX, USA) are used to monitor the current output of each channel. A strain-gauge interface front-end that features a precision 24-bit analog-to-digital-converter (ADC, ADS1220IPW, Texas Instruments, Dallas, TX, USA) and an active shielding driver (OPA376, Texas Instruments, Dallas, TX, USA) powered by a separate low-noise power conditioning chip (TPS79301, Texas Instruments, Dallas, TX, USA) is implemented for the strain-gauge installed on the base spring (CEA-06-250UTA-350, Micro Measurements, Raleigh, NC, USA). A commercial inertial measurement unit (IMU) protoboard (ISM303DHCX, Adafruit Industries, New York, NY, USA) is employed for kinematics estimation purposes. To control all the drivers and peripherals on the board, a 32-bit commercial prototyping microprocessor board (Teensy 4.1, PJRC, Portland, OR, USA) is utilized, which enhances system accessibility and faster development. The embedded system can operate at a bandwidth of up to 2 kHz for optimal communication with sensors and actuators, and can be adjusted based on the desired control algorithm. During the included experiments the system ran at 500 Hz. The embedded system runs on an input voltage range of 6–24 V, and is powered by a four-cell (14.8 V) lithium polymer battery with a 650 mAh capacity. To operate the system's digital/analog peripherals, a wide-range switched-mode power supply (LMR50410Y-Q1, Texas Instruments, Dallas, TX, USA) is employed to reduce the voltage level. The systems overall dimensions are efficient and compact, at 83.95 × 43.94 mm.

3) Baseline Control Architecture: To increase efficiency of the variable stiffness ankle, we limit the activation of the solenoid actuators to instances when a state transition is required. To ensure safety of the device, the actuator should remain locked when the variable stiffness ankle prosthesis is in the stance phase of the gait and bearing the subject's weight. To implement these requirements, we incorporated a finite state machine (FSM) in the low-level controller as depicted in Fig. 7. When a command is sent from the controller to engage or disengage a locking actuator, the device reads the strain value from the strain gauge and if this value is less than the strain threshold ϵ_{thresh} indicating that the foot is in swing phase, the state machine enters the pin engaging or disengaging state (State 6 or State 3). During pin actuation a constant voltage is applied to the actuator for the duration of locking based on a time constant (t_{act}), as determined in benchtop validation.

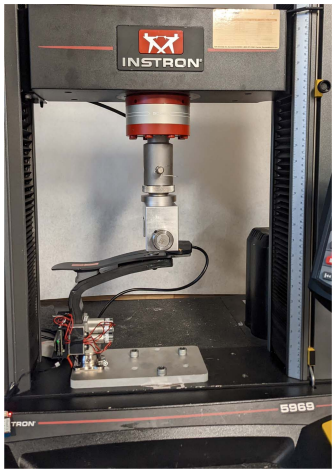

Fig. 8. Benchtop stiffness characterization. Stiffness of the prosthesis was evaluated on a material testing system with a custom test fixture.

III. Device Validation

A. Benchtop Evaluation

1) Stiffness Characterization: We evaluated the stiffness of the prosthesis through benchtop testing performed on a material testing system (Model 5969 Material Testing System, Instron, Norwood, MA). For each of the 32 distinct stiffness settings, the device was loaded to a maximum load of 700 N at a rate of 50 N/s, and deflection of the prosthesis at the point of load application was measured (Fig. 8). A custom test fixture was designed for use with the Instron which applies the load in line with the load cell in order to remove moment induced errors from the Intron. A digital inclinometer (AXISENSE-2 USB90, TE Connectivity, Schaffhausen, Switzerland) is used to measure the angular deflection of the prosthesis during benchtop testing.

2) Stress Measurements: Stress in the leaf spring was measured with a strain gauge installed on the ground spring. Strain was measured during benchtop testing on the custom Instron test fixture.

3) Actuator Characterization: We performed electromechanical characterization of the actuator with the embedded system operating at a bandwidth of 5 kHz. First, we characterized the minimum required actuation time to engage and disengage the actuator at multiple voltage levels, which will be used as actuation time constants (t_{act}) in the FSM. We then observed the transient current response of the actuator with the determined actuation time constant of the actuator. Total energy consumption analysis was made based on the transient response. The quiescent current and idle power of the embedded system were measured with normal operation frequency at bandwidth of 1 kHz.

B. Pilot Study

1) Experimental Design: This study was approved by the MIT Committee on the Use of Humans as Experimental Subjects (protocol number: 1609692618A010, approval date: November 1, 2018), and written informed consent was obtained. A pilot study was conducted with one study participant (body mass: 82.6 kg, height: 1.83 m, age: 49, time since amputation: 30 years, sex: male) with unilateral below knee amputation. During the experiment the subject walked on an instrumented treadmill (FIT, Bertec, Columbus, OH) at the speeds of 0.75 m/s, 1.0 m/s, 1.25 m/s, and 1.5 m/s for 30 s for each trial (Fig. 9). 28 trials were performed, with the variable stiffness prosthesis at six distinct stiffness states, as well as a standard passive ESR prosthesis of the subject's prescribed size and category (Taleo 27-6, Ottobock, Duderstadt, Germany). The order of the trials for each stiffness state was randomized. A 12-camera motion capture system (Vero, Vicon Industries, Inc., Hauppauge, NY) was used to collect full kinematic data during walking (100 Hz). A custom full-body marker set based on the open source "3DGaitModelwithSimpleArms" marker set was used for kinematic data collection, with five markers on each foot, seven on each shank, seven on each thigh, four on the pelvis, five on the torso, four on each upper arm, four on each lower arm, four on each hand, and five on the head. A split belt treadmill with integrated force plates (FIT, Bertec, Columbus, OH) was used to collect kinetic data (1000 Hz). Data from onboard sensors on the prosthesis (strain gauge, IMU, current sensors) was logged for each trial (500 Hz). The optimal stiffness state for each speed is defined as the VSA stiffness which minimizes contralateral limb EAM, due to the study goal of reducing contralateral limb loading and risk factors for OA development through a variable stiffness device.

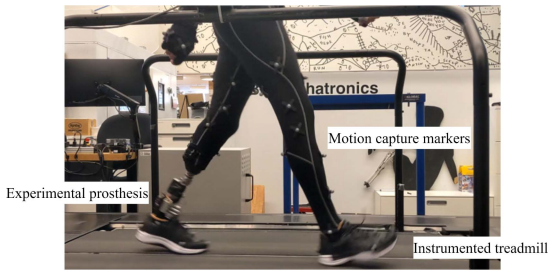

Fig. 9. Experimental platform for biomechanical study. The study participant walked on a split-belt treadmill with integrated force plates with the developed prosthesis.

2) Data Analysis: We processed the data using OpenSim (OpenSim 4.3, Simbios, Stanford, CA) and AddBiomechanics [37]. The markerset is scaled to match mass and inertial properties standard residual limb dimensions and properties [38]. We adjusted the mass of the lower leg segment for each trial to reflect the difference in mass between the variable stiffness device and the ESR device. Optimal scaling of the subject specific model and inverse kinematics are conducted in AddBiomechanics [37]. Inverse dynamics are performed using OpenSim (OpenSim 4.3, Simbios, Stanford, CA). A 3rd order zero-lag low-pass Butterworth filter was used to filter kinematic (6 Hz) and kinetic (12 Hz) data. The data was segmented into individual gait cycles for each trial, and gait cycles were excluded if the force and torque data was greater than two standard deviations from the mean value.

TABLE II
DEVICE MASS

Component	Mass (g)	Qty
Leaf springs	370	1
Housing	170	1
Battery	78	1
Hardware	67	Various
Pyramid adapter	53	1
Embedded system	37	1
Actuator assembly	26	5
Urethane bumper	22	1
Electronics case	18	1
Total	**945**	

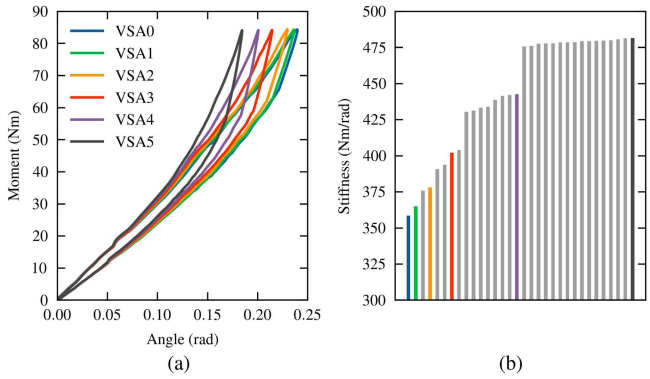

Fig. 10. Stiffness range of variable stiffness prosthesis. (a) Moment versus angular displacement curves of variable stiffness ankle–foot prosthesis from benchtop validation, (b) rotational stiffness of VSA at each stiffness state.

IV. RESULTS

The following section presents results from benchtop device validation experiments and human subject testing.

A. Device Validation

1) Mechanical Characteristics: The mass of the device is presented in Table II. The total device mass of 945 g includes the battery and electronics, and excludes the cosmetic foot cover. Max stress in the leaf springs was measured directly from a strain gauge mounted on the ground spring during bench top testing to validate mechanical modeling results of the spring design. A maximum strain of 0.16% was measured, corresponding to a maximum stress value of 210 MPa. Fig. 10(a) shows the torque angle plot of the variable stiffness ankle prosthesis from the data collected during benchtop Instron testing. Fig. 10(b) shows the corresponding stiffness for each independent stiffness state. There are 32 distinct stiffness states, with the range of stiffnesses from lowest to highest stiffness settings creating a 36% increase in joint stiffness of the ankle for the evaluated maximum load condition. The target stiffness range of 352 Nm/rad–479 Nm/rad was validated during benchtop testing. The discrete stiffness change varies between stiffness settings, the number of discrete settings with a stiffness change of 2 Nm/rad or greater from the

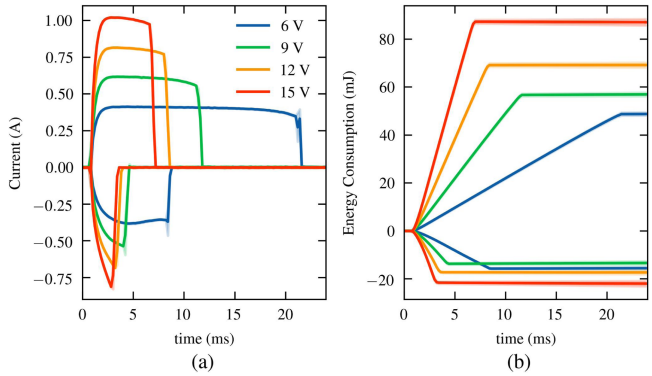

Fig. 11. Electrical transient characteristics of the actuator. (a) Transient current response of linear actuator for a given voltage level. (b) Accumulated transient energy consumption of the actuator for a given voltage level.

subsequent setting is 15. The resolution of stiffness adjustment varies from 0.1 to 33 Nm/rad.

2) Electromechanical Characteristics: Table III summarizes the electromechanical characteristics of the system. The measured minimum actuation times were than used as actuation time constants (t_{act}) in the low-level FSM. A higher actuation voltage corresponds to faster actuation and higher actuation force, while actuation current levels increased proportionally to actuation voltage. A higher input voltage for the embedded system consumes greater idle energy due to the efficiency difference of the input-stage switched mode power supply converter. During actuation, a higher input voltage generally consumes more energy, although 9 V input voltage consumes less energy during actuator engagement than 6 V. Fig. 11 shows the transient electrical response of the actuator.

B. Clinical Pilot Study Results

The variable stiffness prosthesis demonstrates an increase in peak joint angle, increase in energy return, increase in peak power, and a decrease in contralateral limb external adduction moment for each walking speed compared to the passive prosthesis.

1) Joint Angle: We see an increase in maximum joint angle of the prosthesis across speeds for the VSA compared to the passive device. The optimal VSA stiffness at each speed shows an increase in range of motion of 22.2%, 19.8%, 6.1%, and 28.7% at 0.75 m/s, 1.0 m/s, 1.25 m/s, and 1.5 m/s, respectively. Fig. 12(a) shows maximum joint angle for each of six representative stiffness settings on the VSA compared to the passive device at the evaluated walking speeds (0.75 m/s, 1.0 m/s, 1.25 m/s, and 1.5 m/s). Fig. 13(a) presents mean joint angle across gait cycle for the optimal VSA stiffness compared to the passive ESR device.

2) Peak Ankle Power: The VSA optimal stiffness compared to the passive device demonstrates an increase in peak power of 23.8%, 15.0%, –14.4%, and 8.7% at 0.75 m/s, 1.0 m/s, 1.25 m/s, and 1.5 m/s, respectively. Fig. 12(b) shows peak joint power for each of six representative stiffness settings on the VSA compared

TABLE III
SUMMARY OF ELECTROMECHANICAL CHARACTERISTICS

Voltage (V)	T Engage t_{act} (ms)	T Disengage t_{act} (ms)	Peak current Engage (mA)	Peak current Disengage (mA)	E Engage (mJ)	E Disengage (mJ)	Quiescent Current (mA)	Idle Power (mW)
6	7.6	20.4	382	413	15.5	48.8	99	594
9	3.4	10.6	537	617	13.45	56.9	71	638
12	2.6	7.4	685	815	17.3	69.2	57	684
15	2	5.8	813	1020	22.0	87.0	47	705

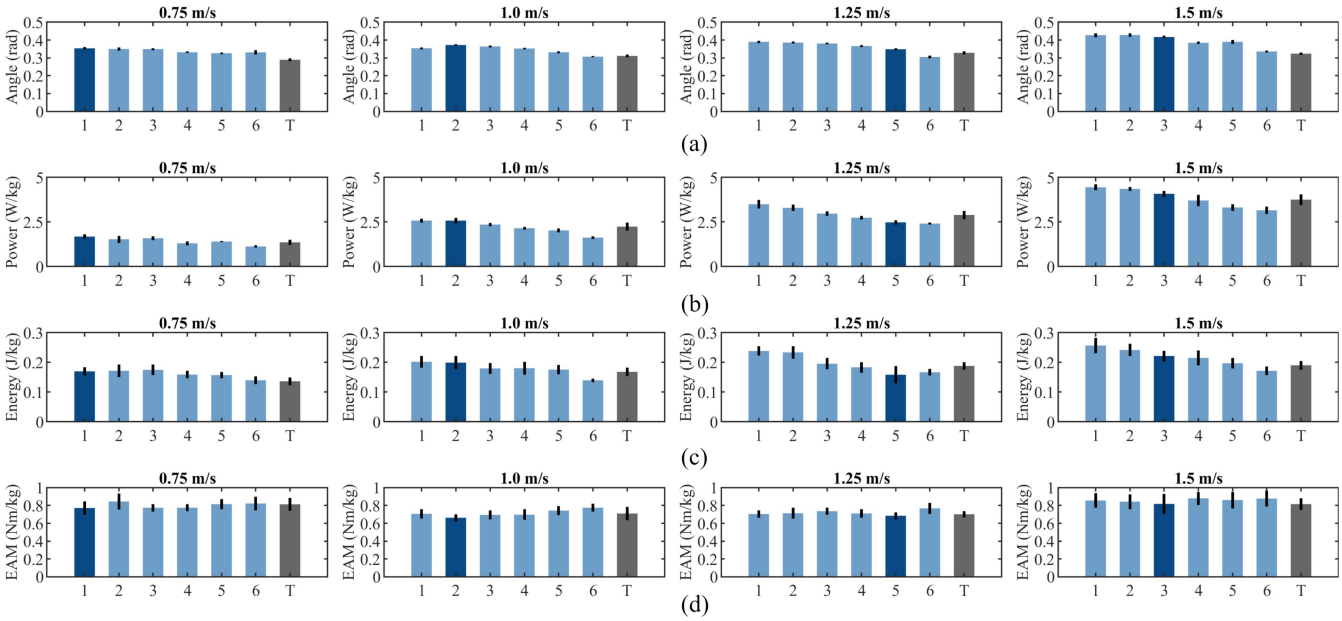

Fig. 12. Metrics of interest across speeds for all stiffnesses. Metrics of interest across speeds for each evaluated VSA stiffness (1–6) in blue compared to prescribed passive prosthesis in grey. The optimal stiffness which minimizes leading limb external adduction moment is shown in dark blue. Error bars represent ± 1 standard deviation. (a) Maximum joint angle. (b) Peak power. (c) Energy return, and (d) 1st Peak of leading limb external adduction moment.

to the passive device at the evaluated walking speeds (0.75 m/s, 1.0 m/s, 1.25 m/s, and 1.5 m/s). Fig. 13(b) presents mean joint power across gait cycle for the optimal VSA stiffness compared to the passive ESR device.

3) Energy Return: We see an increase in energy return across speeds for the VSA compared to the passive device. The optimal VSA stiffness at each speed shows an increase in energy return of 25.7%, 18.3%, –15.8%, and 16.5% at 0.75 m/s, 1.0 m/s, 1.25 m/s, and 1.5 m/s, respectively. Fig. 12(c) shows total energy return for each of the six representative stiffness settings on the VSA compared to the passive device at the evaluated walking speeds (0.75 m/s, 1.0 m/s, 1.25 m/s, and 1.5 m/s). Fig. 13(c) presents mean stored energy across gait cycle for the optimal VSA stiffness compared to the passive ESR device.

4) Contralateral Limb External Adduction Moment: The results from our pilot study demonstrate a decrease in contralateral limb knee EAM across speeds. The optimal VSA stiffness at each speed shows a decrease in EAM of 5.2%, 6.8%, 2.5%, and 0.3% at 0.75 m/s, 1.0 m/s, 1.25 m/s, and 1.5 m/s, respectively. Fig. 12(d) shows the first peak of contralateral knee EAM for each of six representative stiffness settings on the VSA compared to the passive device at the evaluated walking speeds (0.75 m/s, 1.0 m/s, 1.25 m/s, and 1.5 m/s). Fig. 13(d) presents mean EAM across gait cycle for the optimal VSA stiffness compared to the passive ESR device.

V. DISCUSSION

A. Device Evaluation

The benchtop testing results demonstrate that the device successfully achieves the targeted stiffness range, device mass, and structural integrity. The benchtop stiffness characterization of the system demonstrates the high-resolution stiffness control of the prosthesis. The msreaass of the variable stiffness prosthesis is lower than all existing commercial quasi-passive devices, and lower mass than all research platforms. We demonstrate that the VSA prosthesis successfully matches biological levels of ankle stiffness for a person of our target body mass ranging from a slow walk (0.75 m/s) to a fast walk (1.5 m/s). We also show that the proposed embedded system concept and low-level control architecture can provide stable control of the electromechanical actuators. The results demonstrate that the

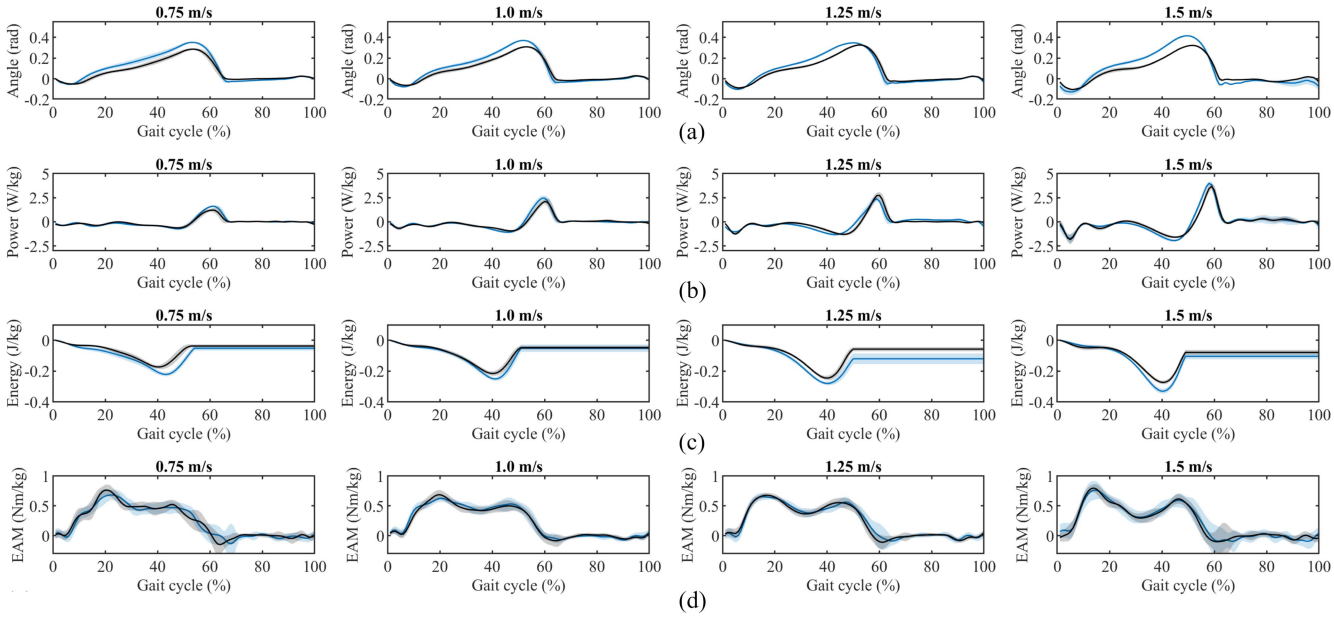

Fig. 13. Pilot study results. Mean values across gait cycles for optimal VSA stiffness (blue) and prescribed passive prosthesis (grey) are shown for (a) prosthesis joint angle, (b) ankle power on prosthesis side, (c) stored energy on the prosthesis side, and (d) external adduction moment of contralateral limb. Shaded regions represent $\pm$ 1 standard deviation.

simplified dynamic model of the actuator provides effective means to construct the control system with minimal sensors. Lower input voltages generally consume less energy in idle state and during transient actuation, while it requires further study to full investigate the relations of them. While the electromagnetic mechanical system shows multiorder complex dynamics, the results demonstrate that the dynamics can be simplified with a constant actuation time and voltage to ensure stable end-state after actuation. The electromechanical evaluation demonstrates that for the selected battery voltage of 12 V, the battery life is approximately 10 h if we assume 1 actuator state change every 10 steps, and 11 hours of standby power. In future iterations of the design, the embedded system can be greatly reduced in size through the use of: 1) an individual IMU chip directly placed on the board; 2) a commercial custom microprocessor; and 3) a single motor driver chip and output-stage MOSFET switches with time-domain multiplexing of driver. Similarly, the continuous power consumption on electronics can be greatly reduced through design optimizations of the electronics.

B. Clinical Pilot Study

The pilot study demonstrates the performance of the variable stiffness ankle during level ground walking at various speeds, providing preliminary evidence of potential advantages of the quasi-passive variable stiffness ankle–foot prosthesis. Pilot study results demonstrate an increased prosthesis range of motion, increase in peak ankle power, increase in stored and returned energy, and a decrease in external adduction moment of the contralateral limb while walking with the variable stiffness prosthesis compared to the passive device, across evaluated walking speeds. The optimal prosthesis stiffness, which we define by the condition which minimizes the first peak of EAM, generally increases with increasing walking speed. This trend agrees with the behavior of the biological ankle–foot complex, which demonstrates an increase in quasi-stiffness as walking speed increases. By optimizing prosthesis stiffness based on walking speed, energy storage and subsequent energy return is increased, leading to increased peak power in a quasi-passive device. This is an exciting result that demonstrates the importance of maximizing energy storage in passive or quasi-passive devices in order to decrease unwanted contralateral limb loading. This result could have important implications for how prostheses are designed, and demonstrates the importance of adaptable prosthesis stiffness.

C. Limitations and Future Work

Limitations of the presented variable stiffness prosthesis include resolution and nonlinearity of stiffness adjustment and the preliminary nature of the presented pilot study results. The designed variable stiffness prosthesis utilizes discrete stiffness control, a potential tradeoff compared to the existing variable stiffness devices which allow for continuous stiffness selection (Table I). Additionally, the stiffness resolution is nonlinear over the range of possible stiffness settings, ranging from 0.1 to 33 Nm/rad, with 15 of the 32 possible stiffness states allowing for a stiffness increase of 2 Nm/rad or greater from the subsequent setting. However, prior research has demonstrated that the smallest stiffness change detectable by prosthesis users is 7% [39]. As such, we hypothesize that the discrete stiffness setting of the presented variable stiffness which range from 1% to 7%

are sufficient for observing clinical benefits of prosthesis stiffness adjustment and are worth the operating bandwidth, energy return, and low mass and power requirements offered by the design. The resolution of stiffness change as well as the linearity of stiffness adjustment could be tuned in future iterations of the device by optimizing thickness and number of parallel springs. Further benchtop characterization across a larger maximum dorsiflexion angle would provide insight into how the nonlinear stiffness range and resolution may vary for higher loads and greater deflections. The biomechanical results presented in this article are preliminary, as experiments were conducted with one study participant as a pilot study. Further experiments with a larger cohort of study participants are necessary in order to draw conclusions about the effects of the prosthesis on biomechanics of walking and any potential long-term clinical benefits. However, the data collected during the pilot study demonstrate promising initial results and motivate the need for a broader study.

VI. Conclusion

This article presents the first of its architecture variable stiffness ankle–foot prosthesis utilizing a novel locking parallel leaf spring mechanism for stiffness control. This prosthesis design has a lower device mass compared to existing powered and quasi-passive stiffness-varying prostheses, and increases biomimetic functionality beyond standard passive prostheses. We present initial results showing potential benefits of such a device on the walking biomechanics of a person with transtibial amputation. This prosthesis has the potential to expand access to high performance prosthesis technology by creating a device that is low mass, low power, and lower cost compared to fully powered devices. Our work presents promising initial results on the potential impact of a quasi-passive variable stiffness ankle–foot prosthesis for walking and motivates broader studies to further explore the effect of a the variable stiffness prosthesis on the biomechanics and energetics of variable speed walking. Additionally, this device has the potential to enable explorations of the impact of prosthesis stiffness on biomechanics in a variety of scenarios such as across varied terrain, various ground surfaces, and running.

Competing Interests

HMH and ER hold a filed patent entitled "Leaf Spring with High Resolution Stiffness Control," US Application No. 18/044,346, filed Sept. 8, 2021. The authors declare that they have no other competing interests.

Author's Contributions

ER designed and built the prosthesis, designed and ran the clinical trials, analyzed the data, and wrote the manuscript. SHY designed and built the custom embedded system and contributed to writing of the manuscript. CL assisted with electronics fabrication, assisted with data collection, and helped to run the clinical trials. HMH oversaw the work and contributed to ideation of device design and experimental design.

Acknowledgment

The authors would like to thank Ottobock for the fabrication of the custom composite leaf springs, and Michael Nawrot for his contributions on the Vicon Nexus data processing pipeline.

References

[1] K. Ziegler-Graham, E. J. MacKenzie, P. L. Ephraim, T. G. Travison, and R. Brookmeyer, "Estimating the prevalence of limb loss in the United States: 2005 to 2050," *Arch. Phys. Med. Rehabil.*, vol. 89, no. 3, pp. 422–429, 2008.

[2] R. Gailey et al., "Review of secondary physical conditions associated with lower-limb amputation and long-term prosthesis use," *J. Rehabil. Res. Develop.*, vol. 45, no. 1, 2008, Art. no. 15.

[3] P. A. Struyf, C. M. van Heugten, M. W. Hitters, and R. J. Smeets, "The prevalence of osteoarthritis of the intact hip and knee among traumatic leg amputees," *Arch. Phys. Med. Rehabil.*, vol. 90, no. 3, pp. 440–446, 2009.

[4] N. Foroughi, R. Smith, and B. Vanwanseele, "The association of external knee adduction moment with biomechanical variables in osteoarthritis: A systematic review," *Knee*, vol. 16, no. 5, pp. 303–309, 2009.

[5] A. Mündermann, C. O. Dyrby, and T. P. Andriacchi, "Secondary gait changes in patients with medial compartment knee osteoarthritis: Increased load at the ankle, knee, and hip during walking," *Arthritis Rheumatism*, vol. 52, no. 9, pp. 2835–2844, 2005.

[6] D. C. Morgenroth et al., "The effect of prosthetic foot push-off on mechanical loading associated with knee osteoarthritis in lower extremity amputees," *Gait Posture*, vol. 34, no. 4, pp. 502–507, 2011.

[7] Z. Ding, H. L. Jarvis, A. N. Bennett, R. Baker, and A. M. Bull, "Higher knee contact forces might underlie increased osteoarthritis rates in high functioning amputees: A pilot study," *J. Orthopaedic Res.*, vol. 39, no. 4, pp. 850–860, 2021.

[8] G. Bovi, M. Rabuffetti, P. Mazzoleni, and M. Ferrarin, "A multiple-task gait analysis approach: Kinematic, kinetic and emg reference data for healthy young and adult subjects," *Gait Posture*, vol. 33, no. 1, pp. 6–13, 2011.

[9] M. Vlutters, T. Boonstra, A. C. Schouten, and H. van der Kooij, "Direct measurement of the intrinsic ankle stiffness during standing," *J. Biomech.*, vol. 48, no. 7, pp. 1258–1263, 2015.

[10] M. K. Shepherd and E. J. Rouse, "The vspa foot: A quasi-passive ankle-foot prosthesis with continuously variable stiffness," *IEEE Trans. Neural Syst. Rehabil. Eng.*, vol. 25, no. 12, pp. 2375–2386, Dec. 2017.

[11] J. D. Lee, L. M. Mooney, and E. J. Rouse, "Design and characterization of a quasi-passive pneumatic foot-ankle prosthesis," *IEEE Trans. Neural Syst. Rehabil. Eng.*, vol. 25, no. 7, pp. 823–831, Jul. 2017.

[12] C. Lecomte, A. L. Ármannsdóttir, F. Starker, H. Tryggvason, K. Briem, and S. Brynjolfsson, "Variable stiffness foot design and validation," *J. Biomech.*, vol. 122, 2021, Art. no. 110440.

[13] S. H. Collins and A. D. Kuo, "Recycling energy to restore impaired ankle function during human walking," *PLoS one*, vol. 5, no. 2, 2010, Art. no. e9307.

[14] F. Heremans, S. Vijayakumar, M. Bouri, B. Dehez, and R. Ronsse, "Bio-inspired design and validation of the efficient lockable spring ankle (ELSA) prosthesis," in *Proc. IEEE 16th Int. Conf. Rehabil. Robot.*, 2019, pp. 411–416.

[15] D. A. Winter, "Energy generation and absorption at the ankle and knee during fast, natural, and slow cadences," *Clin. orthopaedics Related Res.*, no. 175, pp. 147–154, 1983.

[16] K. Shamaei, G. S. Sawicki, and A. M. Dollar, "Estimation of quasi-stiffness and propulsive work of the human ankle in the stance phase of walking," *PLoS one*, vol. 8, no. 3, 2013, Art. no. e59935.

[17] D. J. Farris and G. S. Sawicki, "The mechanics and energetics of human walking and running: A joint level perspective," *J. Roy. Soc. Interface*, vol. 9, no. 66, pp. 110–118, 2012.

[18] W. L. Childers and K. Z. Takahashi, "Increasing prosthetic foot energy return affects whole-body mechanics during walking on level ground and slopes," *Sci. Rep.*, vol. 8, no. 1, pp. 1–12, 2018.

[19] K. E. Zelik et al., "Systematic variation of prosthetic foot spring affects center-of-mass mechanics and metabolic cost during walking," *IEEE Trans. Neural Syst. Rehabil. Eng.*, vol. 19, no. 4, pp. 411–419, 2011.

[20] N. P. Fey, G. K. Klute, and R. R. Neptune, "Altering prosthetic foot stiffness influences foot and muscle function during below-knee amputee walking: A modeling and simulation analysis," *J. Biomech.*, vol. 46, no. 4, pp. 637–644, 2013.
[21] A. M. Grabowski and S. D' Andrea, "Effects of a powered ankle-foot prosthesis on kinetic loading of the unaffected leg during level-ground walking," *J. NeuroEngineering Rehabil.*, vol. 10, pp. 1–12, 6 2013.
[22] Ottobock, "Meridium." Accessed: May 23, 2023. https://www.ottobockus.com/products/meridium/
[23] Blanchford, "Elan." Accessed: May 23, 2023. https://www.blatchfordus.com/products/elan/
[24] Fillauer, "Raize microprocessor foot." Accessed: May 23, 2023. https://fillauer.com/wp-content/uploads/2020/02/Lower-Extremity-Catalog-2020.pdf
[25] A. M. Willson et al., "Evaluation of a quasi-passive biarticular prosthesis to replicate gastrocnemius function in transtibial amputee gait," *J. Biomech.*, vol. 129, 2021, Art. no. 110749.
[26] Össur, "Prioprio foot." Accessed: May 23, 2023. https://www.ossur.com/en-us/prosthetics/feet/proprio-foot
[27] T. Lenzi, M. Cempini, L. J. Hargrove, and T. A. Kuiken, "Design, development, and validation of a lightweight nonbackdrivable robotic ankle prosthesis," *IEEE/ASME Trans. Mechatron.*, vol. 24, no. 2, pp. 471–482, Apr. 2019.
[28] E. A. Rogers, M. E. Carney, S. H. Yeon, T. R. Clites, D. Solav, and H. M. Herr, "An ankle-foot prosthesis for rock climbing augmentation," *IEEE Trans. Neural Syst. Rehabil. Eng.*, vol. 29, pp. 41–51, Feb. 2021.
[29] H. L. Bartlett, S. T. King, M. Goldfarb, and B. E. Lawson, "A semi-powered ankle prosthesis and unified controller for level and sloped walking," *IEEE Trans. Neural Syst. Rehabil. Eng.*, vol. 29, pp. 320–329, Mar. 2021.
[30] E. M. Glanzer and P. G. Adamczyk, "Design and validation of a semi-active variable stiffness foot prosthesis," *IEEE Trans. Neural Syst. Rehabil. Eng.*, vol. 26, no. 12, pp. 2351–2359, Dec. 2018.
[31] R. D. Budynas and J. K. Nisbett, "Deflection of curved members," *Shigley's Mechanical Engineering Design*, New York:McGraw Hill, pp. 164–165, 2011.
[32] International Organization for Standardization: *Prosthetics-Structural Testing of Lower-Limb Prostheses - Requirements and Test Methods*, ISO-10328, 2016.
[33] B. F. Sørensen and S. Goutianos, "Prediction of fatigue limit for unidirectional carbon fibre/epoxy composites," in *IOP Conf. Series: Mater. Sci. Eng.*, vol. 388, no. 1. IOP Publishing, 2018, Art. no. 012017.
[34] N. Morita, Y. Mino, N. Yoshikawa, and M. Hojo, "Versatile fatigue strength evaluation of unidirectional cfrp specimen based on micro-stress analysis of resin," *Composite Structures*, vol. 276, 2021, Art. no. 114539.
[35] R. G. Solutions, "Virgin PTFE material specification sheet," 2008. Accessed: May. 23, 2023. https://www.ramgaskets.com/wp-content/uploads/2020/08/Virgin-PTFE.pdf
[36] K. Johnson, "Normal Contact of Elastic Solids: Hertz Theory," *Contact Mechanics*, Cambridge University Press, pp. 84–107, 1985.
[37] K. Werling et al., "Rapid bilevel optimization to concurrently solve musculoskeletal scaling, marker registration, and inverse kinematic problems for human motion reconstruction," *bioRxiv*, 2022.
[38] A. M. Willson et al., "Full body musculoskeletal model for simulations of gait in persons with transtibial amputation," *Comput. Methods Biomech. Biomed. Eng.*, pp. 1–12, 2022.
[39] M. K. Shepherd, A. F. Azocar, M. J. Major, and E. J. Rouse, "Amputee perception of prosthetic ankle stiffness during locomotion," *J. neuroengineering Rehabil.*, vol. 15, no. 1, pp. 1–10, 2018.

Emily Rogers-Bradley received the S.B. degree from Harvard University, MA, USA, in 2015 and the S.M. and the Ph.D. degrees in mechanical engineering from the Massachusetts Institute of Technology (MIT), MA, USA, in 2019 and 2023, respectively.

She was a Member of the K. Lisa Yang Center for Bionics and the MIT Biomechatronics Lab, MIT. She is currently an Assistant Professor in mechanical and biomedical engineering and the Director of the Adaptive Bionics Lab, University of Calgary, Calgary, AB, Canada.

Seong Ho Yeon received the S.M. degree in media arts and sciences from the Massachusetts Institute of Technology (MIT), MA, USA, in 2019, where he is currently working toward the Ph.D. degree in program in media arts and sciences with the MIT Media Lab.

He is a Graduate Research Fellow with K. Lisa Yang Center for Bionics, MIT.

Christian Landis received the Sc.B. degree in biomedical engineering from Brown University, RI, USA, in 2020. He is currently working toward the M.S. degree in electrical and computer engineering with Johns Hopkins University, MD, USA.

He is a Member of the K. Lisa Yang Center for Bionics and the MIT Biomechatronics Lab, Massachusetts Institute of Technology (MIT), MA, USA.

Hugh M. Herr received the B.A. degree in physics from Millersville University of Pennsylvania, PA, USA, in 1990, the S.M. degree in mechanical engineering from Massachusetts Institute of Technology (MIT), MA, USA, in 1993, and the Ph.D. degree in biophysics from Harvard University, MA, USA, in 1998.

He is a Professor of media arts and sciences with the MIT Media Lab, co-Director of the K. Lisa Yang Center for Bionics, and Director of the MIT Biomechatronics Lab, MIT, MA, USA. He has authored or coauthored more than 250 peer-reviewed manuscripts and patents, and his inventions include active leg exoskeletons, powered ankle-foot prostheses, and interfacing technologies.